MIT Open Access Articles

Nanochemo-mechanical signature of organic-rich shales: a coupled indentation–EDX analysis

1 **Nano-Chemomechanical Signature of Organic-Rich Shales: A Coupled Indentation-**

2 **EDX Analysis**

3 By: Sara Abedi[1,*,**], Mirna Slim[1], Ronny Hofmann[2], Taras Bryndzia[2] and Franz-Josef Ulm[1]

4

5 [1] Department of Civil and Environmental Engineering, Massachusetts Institute of
6 Technology, Cambridge, MA.
7 [2] Shell International Exploration and Production, Projects & Technology, Houston, TX.

8

9

10 ## Abstract

11 The organic-inorganic nature of organic-rich source rocks poses several challenges for
12 the development of functional relations that link mechanical properties with geochemical
13 composition. With this focus in mind, we herein propose a method that enables chemo-
14 mechanical characterization of this highly heterogeneous source rock at the micron and
15 submicron length scale through a statistical analysis of a large array of Energy Dispersive
16 X-Ray Spectroscopy (EDX) data coupled with nanoindentation data. The ability to
17 include elemental composition to the indentation probe via EDX is shown to provide a
18 means to identify pure material phases, mixture phases and interfaces between different
19 phases. Employed over a large array, the statistical clustering of this set of chemo-
20 mechanical data provides access to the properties of the fundamental building blocks of
21 clay-dominated organic-rich source rocks. The versatility of the approach is illustrated
22 through the application to a large number of source rocks of different origin, chemical
23 composition and organic content. We find that the identified properties exhibit a unique
24 scaling relation between stiffness and hardness. This suggests that organic-rich shale
25 properties can be reduced to their elementary constituents, with several implications for
26 the development of predictive functional relations between chemical composition and
27 mechanical properties of organic-rich source rocks such as the intimate interplay between
28 clay packing, organic maturity, and mechanical properties of porous clay/organic phase.

31 * Corresponding Author: sara.abedi@pe.tamu.edu

32 ** Now at Harold Vance Department of Petroleum Engineering, Texas A&M University,
33 College Station, TX

34

1. Introduction

Geomaterials such as organic rich shales, can be considered as multiphase and multiscale material systems [17] with intrinsic heterogeneity in chemical composition (including organic diversity (namely maturity) and mineralogy), microtexture and mechanical properties [8]. An improved understanding of fundamental poroelasticity and strength behavior of organic rich shales can lead to development of predictive models that overcome the demand for costly and time-consuming detailed experiments to access their mechanical behavior. For this purpose, it is instructive to explore the complex mechnanical properties of organic rich source rocks at multiple scales, as shown in Figure 1.

Level II corresponds to the characteristic size in the sub-millimeter and millimeter range and is the scale of conventional understanding of organic rich shales regarding their anisotropic poromechanics (Fig. 1). Level I is the scale of porous clay composite intermixed with organic matter. This scale is the scale of nanoindentation and advanced observational methods such as SEM and EDX and is the level of study in this investigation. Level I is of particular importance since porous clay/organic composite is considered as the main driver of macroscopic behavior of organic-rich shales as clay minerals, their packing density, and organic materials control the mechanical and transport properties of these source rocks [3]. Moreover, there is an increasing evidence that maturity of organic matter influences the texture, anisotropy, and ductility of these organic-rich source rocks [46-47]. Finally, level 0 corresponds to the scale of the elementary solid clay particles that make the solid clay phase in organic-rich shales. It should be mentioned that the multi-scale approach followed in this work can be applied to other geomaterials provided that the different scales satisfy the scale separability condition [17].

Following the aforementioned multi-scale structure model and in order to ful-fill the material science paradigm, that is to relate chemical composition, microstructural features, and mechanical performance, the chemo-mechanical properties at fundamental length sacles need to be fully characterized. Advanced characterization techniques have been used to study distinct features of heterogeneous geomaterials at nanometer and micrometer length scales. For instance, valuable insight into the heterogeneity of microstructural features has been obtained by synchrotron x-ray analysis [33, 57-58] small angle neutron scattering [27], and advanced imaging by scanning electron microscopy (SEM) and transmission electron microscopy (TEM) [4, 25, 28]. Similarly, the heterogeneity of mechanical properties has been studied by Atomic force microscopy (AFM) and instrumented indentation on organic-free shale materials [45, 7, 52, 54, 60-61, 3] and organic/inorganic phases in oil and gas bearing shales [2, 39, 59]. Yet, a characterization method that (1) integrates geochemical and mechanical properties in the assessment of organic-rich shale properties, and (2) is able to handle the high heterogeneity of the rock remains to be developed. The method proposed in this paper aims at such a chemo-mechanical characterization of organic-rich shales at micrometer and sub-micrometer length scales (level I) using coupled nanoindentation and energy dispersive x-ray spectroscopy (EDX). The approach herein proposed is an extension to previous approaches developed for inorganic (organic-free) caprocks [12] and cements

79 [9, 30]. Specifically, the original idea advanced in this investigation is that the extensive
80 data sets obtained by both chemical and mechanical testing techniques at the same
81 location and at similar length scales lend themselves to an effective chemo-mechanical
82 clustering analysis to resolves spatial, chemical and mechanical heterogeneities in the
83 form of chemo-mechanical phases present within the probed region.

84 The paper is organized as follows: Section 2 presents the studied materials and the
85 different techniques employed for both chemo-mechanical data acquisition (EDX,
86 nanoindentation) and data analysis by means of clustering at micrometer and sub-
87 micrometer length scales of organic-rich source rocks. The results that can be obtained
88 with this coupled indentation-EDX experiments are discussed in details in Section 3 for a
89 mature gas shale (Haynesville). Finally, in Section 4, the versatility of the approach is
90 illustrated through application to a large range of clay-dominated organic-rich source
91 rocks.

92 **Figure 1 goes here**

93 2. Materials and Methods

94 2.1. Materials

95 Several organic-rich shale samples from major shale reservoirs of different mineralogy
96 and maturity levels were considered in this study (for mineralogy and Total organic
97 content (TOC), see Table 1); namely Haynesville, Marcellus, Fayetteville , Antrim , and
98 Barnett. Clay minerals in these samples were mostly either illite or mixed illite-smectite,
99 with relatively smaller amounts of kaolinite and chlorite. From Rock-Eval analysis,
100 samples from Haynesville, Marcellus, and Fayetteville were identified as mature gas
101 shale samples, whereas samples from Antrim, and Barnett are immature source rocks.
102 The porosity of the samples was either obtained using Gas Research Institute (GRI)
103 protocols (Haynesville) [35-37], or estimated by comparing the bulk densities with the
104 average mineral densities. Based on the mass fraction of material components reported in
105 Table 1, volume fraction of individual solid constituents of samples are obtained. The
106 volume fraction of a particular material constituent k, is determined by:

$$\eta_k = (1 - \phi) \frac{m_k/\rho_k}{\sum_{i=1}^{N} m_i/\rho_i} \tag{1}$$

107 where N represents the number of material phases in the sample, m_i the mass fraction of
108 the solid constituent (Table 1), ρ_i the corresponding mass density (in this study, densities
109 of 2.65-2.82, 2.65, and 2.71 g/cm^3 are considered for clay, quartz and carbonates
110 respectively[Ortega, 2010; www.mindat.org]), and ϕ the porosity obtained
111 experimentally. Table 2 represents the volume fractions of the detected material phases in
112 the studied samples. Clay is the main mineral constituents of these samples with lateral
113 and thickness dimensions of 0.1 - 4 µm and 0.05 - 2 µm; respectively [12, 41]. Regarding
114 the density of organic matter, a variety of values have been used in the literature for
115 organic density, most of which lie in a narrow range. For instance, Mavko et al., [33] has

116 reported a range of 1.1-1.4 g/cc, whereas Vernik and Landis [55] have used a value of
117 1.25 g/cc in their calculations. Taking into account these values, a kerogen density of 1.2
118 g/cc has been assumed in this study.

119 **Table 1 goes here**

120 **Table 2 goes here**

2.2. Sample Preparation

122 Sample surface preparation is essential for surface tests such as nanoindentation and
123 EDX. The surface to be tested should be as smooth as possible and parallel with the
124 bottom surface of the sample. Specifically, trimmed samples of 10 mm diameter and 5
125 mm height were first coarse polished on 400 grit hard perforated pads (TexMet P,
126 Buehler), using an oil-based diamond suspension to prevent chemical reactions. In the
127 next step, samples were dry polished using consecutively 9 μm, 3 μm, and 1 μm
128 aluminum oxide abrasive disks (FibrMet, Buehler). In between polishing steps, the
129 specimens were ultrasonicated in n-decane solution that does not react with the shale
130 minerals, nor with the organic matter. AFM roughness characterization of shale samples
131 prepared with the same procedure showed root-mean-squared (RMS) roughness of 30-
132 150 nm [12, 5]. According to Donnelly et al. (2006), in order to avoid the effects of
133 surface roughness on the results, the obtained indentation depths should be greater than 3
134 times the RMS roughness (450 nm in this study)

2.3. Grid Nanoindentation Technique

136 Instrumented grid indentation provides a tool to characterize the mechanical behavior of a
137 heterogeneous material at sub-micrometer length scales. A large set of indentation tests is
138 carried out on a surface. Each test consists of impinging an indenter tip of known
139 geometry (here, a Berkovich tip with equivalent half-cone angle of 70.32° and curvature
140 radius of approximately 30 nm.) and mechanical properties onto the surface of the
141 material of interest [54, 10, 48], and the mechanical properties of the indented bulk
142 material are extracted from the force-displacement curve (*P-h* curve, Figure 2) by
143 applying a continuum scale model to obtain the indentation modulus *M*, and the
144 indentation hardness *H*:

$$M = \frac{\sqrt{\pi}}{2} \frac{S}{\sqrt{A_c}} \tag{2}$$

$$H = \frac{P}{A_c} \tag{3}$$

145 where P is the measured maximum indentation load, $S = \frac{dP}{dh}$ is the measured initial slope
146 of the unloading branch of the *P-h* curve, and A_c is the projected area of contact between
147 the indenter tip and sample surface, which is determined as a function of the measured
148 maximum indentation depth, h_{max} [43].

149 In this work, each indentation test consisted of a linear increasing load to 4.8 mN in 10 s,
150 followed by a 10 holding phase, and a linear unloading in 10 s. Several indentation grids
151 were performed on samples described in Section 2.1. The spacing between indentation
152 points in each grid is between 3 to 6 micrometer, which provides the required separation
153 between indents. Each grid is composed of 400 to 480 tests making the grids cover
154 surfaces of between 60x60 μm^2 to 120x120 μm^2.

155 **Figure 2 goes here**

156 2.4. Energy Dispersive X-Ray Spectroscopy

157 Energy Dispersive X-Ray Spectroscopy (EDX), a common type of Electron Probe Micro-
158 Analyzer (EPMA) technique, is employed in this study for elemental analysis of organic
159 rich shale samples. The technique utilizes the X-Ray spectrum emitted from the incited
160 solid specimen as a result of a beam of electrons bombarding the sample surface to
161 provide a localized chemical analysis. In EDX, the emitted X-rays are classified based on
162 their energy, and the excited material volume depends on the electron beam energy and
163 material density [23, 49]. One of the most important applications of EDX is elemental
164 mapping which provides spatial distribution of elements of interest over a specific area
165 by collecting X-ray energies of secondary electrons resulting from interaction between an
166 electron beam and a sample. The EPMA technique has been widely used in geology, for
167 instance in the investigation of pore and grain size distributions of individual minerals
168 [40, 31, 15, 50-51].

169 In order to access quantitative elemental composition maps that might represent atomic
170 weight, atomic fractions, actual weight, or atomic ratios of elements, one needs to
171 perform standard quantification at each pixel of quantitative EDX maps [26, 9]. The ratio
172 of mass concentration of the element of interest between the specimen and the standard
173 material is proportional to the ratio of the intensity of a characteristic X-ray measured
174 from the specimen to that emitted from the standard, with the correction which accounts
175 for matrix effects (ZAF) [23, 42]. The measured peak intensities must also be corrected
176 for background and overlap effects.

177 Another way of obtaining elemental composition maps by EDX, is to acquire auto-scaled
178 X-ray intensities from the compositional maps which are generally shown in the
179 commercial EDX softwares. Such compositional maps do not represent quantitative local
180 chemistry at indentation points and the auto-scaled intensity values are used as qualitative
181 indicators of a phase [23, 42, 22]. Applying this method in our chemo-mechanical
182 analysis, and given the uniqueness of the elemental chemical composition of each phase
183 in the studied organic-rich shale samples, each phase can be distinctively linked to one
184 composition of auto-scaled intensity values on average.

185 In this study, EDX maps were acquired with a JEOL JSM-5910 general purpose scanning
186 electron microscope equipped with a Bruker EDX system for elemental analysis. The
187 maps were acquired over the same area on which the nanoindentation grid was
188 performed, and the intensities were averaged around the indentation spots to provide a
189 unique elemental composition for each indentation point on the grid. This elemental
190 analysis was performed with an accelerating voltage of 15 kV, and a working distance of

191 10 mm. While all major constituents relevant for the characterization of gas shale
192 specimens were acquired over the indentation grid, only a reduced number of elemental
193 intensities are required for proper chemo-mechanical phase identification. For instance,
194 for identification of clay-rich phases, these are the Si and Al elemental intensities.

2.5. Length Scale Compatibility in Coupled EDX – Nanoindentaion Analysis

196 An important aspect in coupled EDX-nanoindentation is the compatibility of the
197 characteristic length scales of the voxel assessed respectively by EDX and
198 nanoindentation. In EDX, this length scale is governed by the accelerating voltage. For a
199 15 kV beam voltage, Deirieh et al. (2012) showed from Monte Carlo simulations on
200 common shale constituents such as illite and quartz that such a beam voltage probes
201 elemental intensities at a length scale of L=2~3 μm (Fig. 3). On the other hand, the
202 characteristic voxel size in indentation corresponds approximately to 3-5 times the
203 indentation depth [11, 54]. Thus, in order to probe comparable material volumes by each
204 method, a maximum indentation load of P=4.8 mN was chosen, which leads, for the
205 tested samples, to an average indentation depth of $h_{max} = 400 - 800$ nm. The obtained
206 indentation depths closely satisfy the constraint imposed by surface roughness.

207 **Figure 3 goes here**

2.6. Statistical Approach to Indentation and EDX Experiments for Heterogeneous Materials

210 Natural composite materials are generally very complex, requiring the use of grid
211 indentation and EDX techniques on the material surface. At level I of the organic-rich
212 shales (Fig. 1), the porous clay/organic composite is composed of fine-sized clay particles
213 intermixed with organic matter and nanopores with characteristic length scales d. If the
214 characteristic length of the probed volume l is such that $d<<l$, the chemo-mechanical
215 experiment will sense the on-average homogenized properties of the probed material
216 volume. Moreover, the characteristic length scale of the experiments, l, need to be
217 smaller than the silt-size inclusions $l<<D$ to access the properties of the matrix material
218 and the inclusions. Because of the small-sized clay structures comparing to the probed
219 material volume, the standard EMPA technique can not be used to analyze the exact
220 compositional features of clay particles. The proposed experimental approach can only
221 obtain the on-average porous clay/organic chemo-mechanical properties across different
222 locations on the organic-rich shale matrix.

223 The analysis of chemo-mechanical properties of such heterogenous material requires the
224 use of statistical analysis of the generated experimental data. In this type of analysis, it is
225 also necessary to acquire a large number of indents in order to avoid sampling effects,
226 which demands the use of an adequately large testing surface comparing to the size of
227 distinct material phases of interest.

228 A multi-variate cluster modeling approach is used for statistical analysis of the collected
229 mechanical and chemical data. Through this method, one can identify the most likely
230 number of clusters in a data set, as well as the uncertainty of observations belonging to a
231 cluster based on statistical criteria. The cluster modeling considers each event

232 (comprising nanoindentation and EDX measurements) to be a realization of the random
233 multi-dimensional vector $= (X_i^T, \dots, X_n^T)$, where n is the total number of events (i.e. total
234 number of grid indents). The multi-dimension corresponds to the indentation modulus
235 (M) and hardness (H) as well as chemical components obtained from EDX, which were
236 measured for each of the n tests. The probability density function $f(x_i)$ of the observed
237 data x_i in X_i in a G-component mixture is:

$$f(x_i, \Psi) = \sum_{k=1}^{G} \tau_k \, \phi(x_i, \mu_k, \Sigma_k) \tag{4}$$

238 where τ_k is the probability that an observation belongs to the k-th component ($\sum_{k=1}^{G} \tau_k =$
239 1), $\Psi = (\tau_1, \dots, \tau_k, \xi^T)^T$ with ξ containing the (unknown) group mean, μ_k, and the
240 covariance matrix, Σ_k, and $\phi(x_i, \mu_k, \Sigma_k)$ corresponding to the multi-variate normal
241 density:

$$\phi(x_i, \mu_k, \Sigma_k) = \frac{exp\left(-\frac{1}{2}(x_i - \mu_k)^T (\Sigma_k)^{-1}(x_i - \mu_k)\right)}{\sqrt{det\,(2\pi\Sigma_k)}} \tag{5}$$

242 The best model is obtained by fitting models with differing parameterization and/or
243 number of components to the data by maximum likelihood, and then by implementing a
244 statistical criterion for model selection, here the Bayesian Information Criteria, BIC. The
245 reader is referred to [19-21] for a detailed discussion of clustering analysis. In this study,
246 the open source R package Mclust (http://www.stat.washington.edu/ mclust), well
247 suited for normal mixture modeling and model-based clustering, was employed. The
248 package provides functions for mixture modeling and implements maximum likelihood
249 estimation and Bayesian Information Criteria (BIC) to identify the most likely model and
250 the number of clusters.
251

252 ## 3. Results

253 ### 3.1. Coupled EDX-Grid Nanoindentation Technique

254 To illustrate the added value of enriching mechanical data by chemical data for a
255 statistical phase identification, a comparison of cluster analysis obtained respectively
256 without (Fig. 4) and with (Fig. 5) the EDX analysis is of interest. This comparison is
257 illustrated in Figures 4-6 for one grid on Haynesville shale, but similar results were
258 obtained for other grids and other shale rocks as well. Specifically, while the pure
259 mechanical clustering (Fig. 4) identifies only two phases, the coupled chemo-mechanical
260 clustering picks up four phases of distinct chemo-mechanical properties. The difference
261 in number of phases and properties is recognized from a comparison of the phase maps
262 shown in Figure 6. In contrast to the pure mechanical phases (Fig. 6a), the coupling with
263 chemistry allows one to distinguish bulk phases from mixture phases (Fig. 6b). In
264 particular, by incorporating maps of "Si" and "Al" from EDX into the clustering analysis,
265 phase 1 is identified as a "clay-rich" phase. Similarly, incorporating 'Ca' maps in the

266 clustering provides a means to identify phases 3 and 4 as "calcite-rich" and "quartz-rich"
267 phases, respectively; whereas phase 2 is identified as a mixture phase at the interface
268 between clay-rich and calcite-rich regions. Thus far, the coupled EDX-grid indentation
269 technique provides a means to match mineralogy with mechanical stiffness and strength
270 properties. It is, however, emphasized, that the coupled chemo-mechanical approach only
271 accounts for inorganic elements. That is, the phases thus identified will certainly include
272 the organic phases as well.

273   **Figure 4 goes here**

274   **Figure 5 goes here**

275   **Figure 6 goes here**

276

277   **3.2 Comparison with Bulk Mineralogy**

278 The clustering algorithm also provides volume fractions of the clay-rich and calcite-rich
279 regions on a grid. It should be noted, however, that due to the heterogeneity of the sample
280 a single grid size of 60x60 μm^2 to 120x120 μm^2 may not be representative of the bulk
281 mineralogy, and that several grids are typically required for the volume fractions to
282 converge toward the bulk mineralogy. This is shown in Figure 7: As the number of tests
283 increases, the volume fractions converge toward the volume fraction of the clay-rich
284 phase determined from bulk mineralogy. Figure 7 represents the results of chemo-
285 mechanical clustering analysis on 17 grids performed on Haynesville samples. From
286 these 17 grids, we randomly draw, without replacement, the volume fraction of clay rich
287 phase of one grid and average these values as the number of grids increased. The
288 procedure was repeated 100 times and the results are presented in Figure 7. As expected,
289 all runs converge to the average volume fraction of the clay rich phases among all 17
290 grids of 43% - a value that needs to be compared with the value available from
291 mineralogy. For this comparison, it should be noted that the phases identified from the
292 chemo-mechanical clustering also include porosity and kerogen. Thus for the sought
293 comparison, the bulk mineralogy (in volume%) needs to be corrected to account for both.

294 To this end, we consider (1) that the porosity is distributed homogeneously in all phases
295 composing the sample, thus considering porosity in both the organic and the inorganic
296 phase; and (2) that the organic matter is mostly concentrated in the clay phase [56, 32,
297 18] (Figure 8, Table 3 presents volume fraction of kerogen in the clay-rich phase for all
298 samples). These assumptions are built on the multiscale model proposed in Figure 1. The
299 first assumption provides a means to assess the volume fractions of porous clay and
300 kerogen (in e.g. Haynesville samples) by dividing the volume percentage of bulk clay and
301 kerogen (Table 2) by the solid volume fraction, $1 - \phi$. For the considered Haynesville
302 samples this provides an average volume fraction of 39% and 6% for the porous clay
303 phase and porous kerogen phase, respectively. The second assumption allows us to
304 simply sum up these two volume fractions, to obtain a total volume fraction of the porous
305 clay/kerogen composite in Haynesville samples of 45%. The value so obtained from
306 mineralogy and porosity measurements compares fairly well with the volume fraction of

307 the clay-rich phases identified by coupled Nanoindentation and EDX of 43%. The
308 successful comparison not only validates our conjecture that the coupled
309 Nanoindentation-EDX method provides a quantitative means to separate chemo-
310 mechanical phases in organic-rich shales. It also supports our hypotheses regarding the
311 distributions of porosity and organic matter in the microstructure of mature samples;
312 namely a self-consistent porosity distribution throughout the system (i.e. same porosity in
313 all phases), and a kerogen phase spatially correlated with the clay phase. This observation
314 is also consistent with observation made by others that showed both an inter-organic
315 porosity and a mineral porosity [29, 34].

316   **Figure 7 goes here**

317   **Figure 8 goes here**

318   **Table 3 goes here**

4. Discussion: The Elementary Building Block of Organic-Rich Source Rocks

321 With the coupled chemo-mechanical experimental method thus in place, it is of interest to
322 extend the analysis to a larger set of organic-rich source rocks, ranging from mature to
323 immature samples. Specifically, we herein address the question of whether the clay-rich
324 phase in different source rocks exhibits some chemo-mechanical functional relations that
325 link mechanical properties to mineralogy, packing fractions and maturity. With this
326 objective in mind, several nanoindentation grids in orthogonal directions were conducted
327 on organic-rich samples described in section 2.1, with X1 and X3 corresponding to the
328 parallel-to-bedding and normal-to-bedding direction, respectively. The porous
329 clay/kerogen phases were identified for each direction (X1 and X3) by the described
330 coupled nanoindentation-EDX techniques.

331 Figures 9 and 10 summarize the indentation results of the porous clay/kerogen phases of
332 the studied samples, in the form of a plot of the mean indentation modulus vs. indentation
333 hardness (Fig. 8), and of (M, H) vs. the clay packing density , $\eta_c = 1 - (\eta_k + \phi)$ (where
334 ϕ is the porosity and η_k is the kerogen volume fraction) and the kerogen volume fraction,
335 η_k (Fig. 9), respectively. The results are also provided in Table 4. The following
336 observations deserve attention:

337   1. The stiffness and hardness values of the clay-rich phases of different formations
338   exhibit –on first order– a power scaling of the form $M \sim H^\alpha$ (Fig. 8), where $\alpha < 1$.
339   This scaling is of some significance if we remind ourselves that the results
340   presented in Figure 9 are obtained from samples with different maturity, total
341   organic content (TOC) (Table 2), and porosity (Table 1). Such a distinct scaling
342   relation is a hallmark of functional relations between *(M, H)* and microtexture
343   quantities, such as clay packing density and kerogen content.
344
345   2. The clay-rich phase exhibits a distinct anisotropy in both stiffness (M) and
346   strength-hardness (H), as values in the X1 direction are typically greater than

347   values in the X3-direction [14]. Specifically, the elastic anisotropy, M_1/M_3
348   (where M_1 and M_3 represent the indentation modulus in X1 and X3 directions,
349   respectively), appears to increase with the clay packing fraction (Fig. 9a), but
350   seems unaffected by the kerogen volume fraction (Fig. 9c). This type of elastic
351   anisotropy is reminiscent of that of organic-free clay-bearing shale materials [52,
352   7], and confirms the idea of an effective chemo-mechanical isolation of the clay-
353   rich phase by the suggested method. On the other hand, the indentation hardness
354   (H) which relates to cohesion and friction of the elementary particles [6] is found
355   to be less affected by the clay packing (Fig. 9b), but strongly affected by the
356   kerogen content. In fact, as the kerogen content increases the difference in
357   hardness in the orthogonal direction decreases (Fig. 9d); in stark contrast to the
358   elastic anisotropy (Fig. 9c). That is, while the micron-scale elasticity scales in
359   first-order with the clay packing, the strength behavior appears to be strongly
360   dependent on the kerogen volume fraction in organic-rich clay-bearing source
361   rocks.
362

363 The two distinct observations merit further exploration. We thus consider another, yet
364 related, quantity: the ratio of indentation modulus over hardness (M/H). For an elastic
365 material, M/H only depends on the indenter geometry, and equals $M/H = 2tan\theta = 5.6$
366 for the Berkovich tip of equivalent half-cone angle θ=70.32° employed in our
367 investigation (for derivation see [11]). Greater values of M/H are indicative of the
368 occurrence of plastic deformation mechanisms, as M/H is homogeneous to the inverse of
369 a yield strain. As such, it is commonly employed, in materials science investigations, as a
370 measure of the ductility (see, for instance, Abdolhosseini Qomi et al., [1]). In Figure 11
371 we thus plot this ductility measure (M/H) as a function of the clay packing (Fig. 11a) and
372 the kerogen content (Fig. 11b). Two competing trends are apparent in these figures;
373 namely (1) a decrease in ductility with decreasing clay packing (Fig. 11a), and (2) an
374 increase in ductility with increasing kerogen content (Fig. 11b). As kerogen volume
375 fraction increases, the ductility also increases till the point that the effect of clay packing
376 density prevails which is a decrease in ductility as clay packing density decreases. This
377 added ductility of the kerogen in an otherwise tightly-packed brittle clay matrix [24], is
378 expected to be more pronounced in immature systems than in mature systems, and
379 appears to us at the origin of the intimate interplay between the organic-inorganic
380 strength-stiffness behavior.

381   **Figure 9 goes here**

382   **Figure 10 goes here**

383   **Figure 11 goes here**

384   **Table 4 goes here**

385
386
387

5. Conclusion

The novel methodology of coupled statistical nanoindentation-EDX clustering analysis herein proposed provides an effective means to isolate different chemo-mechanical phases and their interfaces in organic-rich source rocks at micro-meter and sub-micron scale. The method is based on adding relevant chemical markers to mechanical information in a statistical clustering analysis. If carried out over statistically representative surface areas, the method is capable of providing volume fractions of different material constituents.

The overall picture that emerges from the application of the method to a large array of both mature and immature organic-rich rocks of different porosities, is that the clay-rich phase exhibits a unique scaling relation between stiffness (M) and hardness (H). From exploring correlations between mechanical phase properties and clay packing and kerogen content, it appears to us that this scaling is due to an intimate interplay between the increase in elasticity content with clay packing, and a decrease of strength due to the added ductility of kerogen related to an increase in TOC. While this intimate interplay between clay packing and kerogen maturity still merits further investigation, as evidenced by others [47], and corroborated by our own investigation of mature and immature samples, the method here proposed may turn out invaluable for future investigations that aim at reducing the complexity of organic-rich shales to their elementary constituents, with several implications for the development of predictive functional relations between chemical composition and mechanical properties of organic-rich source rocks.

5. Acknowledgment

7. References

1. Abdolhosseini Qomi, M.J., Krakowiak, K.J., Bauchy, M., Stewart, K.L., Shahsavari, R., Jagannathan, D., Brommer, D.B., Baronnet, A., Buehler, M.J., Yip, S., Ulm, F.-J., Van Vliet, K.J., and Pellenq, R.J-.M. (2014) "Combinatorial molecular optimization of cement hydrates." Nature Communications 5, Article number: 4960, doi:10.1038/ncomms5960

2. Ahmadov, R., Vanorio, T., Mavko, G. (2009) "Confocal laser scanning and atomic-force microscopy in estimation of elastic properties of the organic-rich Bazhenov formation. " Leading Edge Vol. 28(1): 18–23, doi: 10.1190/1.3064141

3. Bennett, KC., Berla, LA., Nix, WD., Borja, RI. (2015) "Instrumented nanoindentation and 3D mechanistic modeling of a shale at multiple scales." Acta Geotechnica Vol. 10 (1): 1-14.

430

431   4. Bennett, RH., O'Brien, NR., Hulbert, MH. (1991) "Determinants of clay and shale
432 microfabric signatures: processes and mechanisms. " In: Bennet, RH., O'Brien, NR.,
433 Hulbert, MH. (eds) "Microstructure of fine grained sediments: from mud to shale. "
434 Springer, New York, pp 5–32

435

436   5. Bobko, C. P. (2008) "Assessing the mechanical microstructure of shale by
437 nanoindentation: The Link between mineral composition and mechanical properties."
438 PhD dissertation, Massachusetts Institute of Technology, Cambridge.

439

440   6. Bobko, C. P., Gathier, B., Ortega, J. A., Ulm, F-J., Borges, L., Abousleiman, YN.
441 (2011) "The nanogranular origin of friction and cohesion in shale—a strength
442 homogenization approach to interpretation of nanoindentation results." International
443 Journal of Numerical and Analytical Methods in Geomechanics Vol. 35(17): 1854-1876,
444 doi: 10.1002/nag.984

445

446   7. Bobko, C., Ulm, F-J. (2008) "The nano-mechanical morphology of shale. " Mechanics
447 of Materials, Vol. 40(4–5): 318–337, doi:10.1016/j.mechmat.2007.09.006

448

449   8. Bustin, R. M. (2012) "Shale gas and shale oil petrology and petrophysics"
450 International Journal of Coal Geology, Vol. 103: 1-2, doi:10.1016/j.coal.2012.09.003

451

452   9. Chen, J. J., Sorelli, L., Vandamme, M., Ulm, F-J., Chanvillard, G. (2010) "A coupled
453 nanoindentation/SEM-EDS study on low water/cement ratio portland cement paste:
454 evidence for C–S–H/Ca(OH)$_2$ nanocomposites" Journal of American Ceramic Society,
455 Vol. 93(5): 1484-1493, doi: 10.1111/j.1551-2916.2009.03599.x

456

457   10. Constantinides, G., Ravi Chandran, K. S., Ulm, F-J., Van Vliet, K. J. (2006) "Grid
458 indentation analysis of composite microstructure and mechanics: Principles and
459 validation" Materials Science and Engineering A, Vol. 430: 189–202,
460 doi:10.1016/j.msea.2006.05.125

461

462   11. Constantinides, G., Ulm, F-J. (2007) "The nanogranular nature of C-S-H" Journal of
463 the Mechanics and Physics of Solids. Vol. 55 (1): 64-90, doi:10.1016/j.jmps.2006.06.003

464

465   12. Deirieh, A. (2011) "Statistical Nano-Chemo-Mechanical Assessment of Shale by
466 Wave Dispersive Spectroscopy and Nanoindentation" S. M. dissertation, Massachusetts
467 Institute of Technology, Cambridge.

468

469   13. Deirieh, A., Ortega, J. A., Ulm, F.-J., and Abousleiman, Y. (2012)
470 "Nanochemomechanical assessment of shale: a coupled WDS-indentation analysis" Acta
471 Geotechnica, 7, 271-295, doi: 10.1007/s11440-012-0185-4

472

473   14. Delafargue A, and Ulm, F.-J. (2004) "Explicit approximations of the indentation
474 modulus of elastically orthotropic solids for conical indentation" Int. J. Solids &
475 Structures 41, 7351-7360, doi:10.1016/j.ijsolstr.2004.06.019

476

477   15. Dilks, A., Graham, SC. (1985) "Quantitative mineralogical characterization of
478   sandstones by back-scattered electron image analysis. "Journal of Sedimentary Petrology
479   Vol. 55(3): 347–355, doi: 10.1306/212F86C5-2B24-11D7-8648000102C1865D
480

481   16. Donnelly, E., Baker, S.P., Boskey, A.L., van der Meulen, M.C.H. (2006) "Effects of
482   surface roughness and maximum load on the mechanical properties of cancellous bone
483   measured by nanoindentation." Journal of Biomedical Materials Research A, Vol. 77 (2):
484   426–435.
485

486   17. Dormieux, L., Kondo, D., & Ulm, F.-J. (2006). "Microporomechanics." Chichester
487   UK: J. Wiley & Sons, doi: 10.1002/0470032006
488

489   18. Fitzgerald, JJ., Hamza, AI., Bronnimann, CE., Dec, SF. (1989) "Solid-state 27 Al and
490   29 Si NMR studies of the reactivity of the aluminum-containing clay mineral kaolinite"
491   Solid State Ionics, Vol. 32–33, Part 1: 378-388
492

493   19. Fraley, C., and Raftery, A.E. (1999) "MCLUST: Software for model-based cluster
494   analysis" Journal of Classification, vol. 16: 297-306, doi: 10.1007/s003579900058
495

496   20. Fraley, C., and Raftery, A.E. (2002) "Model-based clustering, discriminant analysis,
497   and density estimation" Journal of the American Statistical Association, vol. 97: 611-631,
498   doi:10.1198/016214502760047131
499

500   21. Fraley, C., and Raftery, A.E. (2007) "Model-based methods of classification: using
501   the mclust software in chemometrics" Journal of Statistical Software, vol. 18: 1-13,
502   doi:10.1360/jos180001
503

504   22. Friel, JJ., Lyman, ChE. (2006) "X-ray mapping in electron-beam instruments"
505   Microscopy and Microanalysis Vol. 12(1): 2–25, doi: 10.1017/S1431927606060211
506

507   23. Goldstein, J., Newbury, DE., Joy, D., Lyman, Ch., Echlin, P., Lifshin, E., Sawyer, L.,
508   Michael, J. (2007) "Scanning Electron Microscopy and X-ray Microanalysis" 3rd ed.
509   Springer
510

511   24. Hantal, G., Brochard, B., Laubie, H., Ebrahimi, D., Pellenq, R.J.-M., Ulm, F.-J.,
512   Coasne, B. (2014) "Atomic-scale modelling of elastic and failure properties of clays."
513   Molecular Physics 112, 1294-1305, doi:10.1080/00268976.2014.897393
514

515   25. Hornby, BE., Schwartz, LM., Hudson, JA. (1994) "Anisotropic effective-medium
516   modeling of the elastic properties of shales. " Geophysics Vol. 59(10): 1570–1583,
517   doi:10.1190/1.1443546
518

519   26. Hughes, JJ., Trtik, P. (2004) "Micro-mechanical properties of cement paste measured
520   by depth-sensing nanoindentation: a preliminary correlation of physical properties with

521 phase type" Materials Characterization Vol. 53(2-4) 223–231,
522 doi:10.1016/j.matchar.2004.08.014
523
524 27. Jin, L., Rother, G., Cole, DR., Mildner, DFR., Duffy, CJ., Brantley, SL. (2011)
525 "Characterization of deep weathering and nanoporosity development in shale—a neutron
526 study". American Mineralogist Vol. 96(4): 498–512, doi: 10.2138/am.2011.3598
527
528 28. Keller, LM., Holzer, L., Wepf, R., Gasser, P. (2011) "3D geometry and topology of
529 pore pathways in Opalinus clay: Implications for mass transport. " Apllied Clay Sciences
530 Vol. 52(1–2): 85–95, doi:10.1016/j.clay.2011.02.003
531
532 29. King, H. E., Eberle, A. P. R., Walters, C. C., Kliewer, C. E., Ertas, D., Huynh, C.
533 (2015) "Pore architecture and connectivity in gas shale" Energy Fuels, Vol. 29: 1375 –
534 1390.
535
536 30. Krakowiak, K., Wilson, W., James, S., Musso, S., Ulm F.-J. (2015) "Inference of the
537 phase-to-mechanical property link via coupled X-ray spectrometry and indentation
538 analysis: Application to cement-based materials." Cement and Concrete Research 67,
539 271-285, doi:10.1016/j.cemconres.2014.09.001
540
541 31. Krinsley, DH. (1998) "Back-scattered scanning electron microscopy and image
542 analysis of sediments and sedimentary rocks. " Cambridge University Press, Cambridge
543
544 32. Kuila, U., McCarty, DK., Derkowski, A., Fischer, TB., Topór, T., Prasad, M. (2014)
545 "Nano-scale texture and porosity of organic matter and clay minerals in organic-rich
546 mudrocks." Fuel Vol. 135: 359–373, doi:10.1016/j.fuel.2014.06.036
547
548 33. Lonardelli, I., Wenk, H-R., Ren, Y. (2007). "Preferred orientation and elastic
549 anisotropy in shales. " Geophysics Vol. 72(2): D33–D40, doi: 10.1190/1.2435966
550
551 34. Loucks, RG., Reed, RM., Ruppel, SC., & Hammes, U. (2012) "Spectrum of pore
552 types and networks in mudrocks and a descriptive classification for matrix-related
553 mudrock pores" AAPG Bulletin, Vol.96 (6): 1071–1098.
554
555 35. Luffel, D., Guidry, F. (1989). "Core analysis results Comprehensive Study Wells
556 Devonian Shales: Topical Report July 1989" Technical Report Restech Houston, Inc.
557
558 36. Luffel, DL., Guidry, FK. (1992). "New core analysis methods for measuring reservoir
559 rock properties of Devonian shale" Journal of Petroleum Technology, Vol. 44(11) :
560 1184–1190, doi: 10.2118/20571-PA
561
562 37. Luffel, DL., Guidry, F. K., Curtis, JB. (1992). "Evaluation of Devonian shale with
563 new core and log analysis methods" Journal of Petroleum Technology, Vol. 44(11)
564 :1192–1197, doi: 10.2118/21297-PA
565

566   38. Mavko, G., Mukerji, T., Dvorkin, J.(2009). "Rock Physics Handbook: Tools for
567   Seismic Analysis in Porous media" Cambridge University Press.

569   39. Mba, K., Prasad, M., Batzle, M. (2010) "The maturity of organic-rich shales using
570   microimpedance analysis. " SPE annual technical conference and exhibition, Florence,
571   September 19–22, SPE 135569, DOI: 10.2118/135569-MS

573   40. McGee, JJ., Keil, K. (2001) "Application of electron probe microanalysis to the study
574   of geological and planetary materials. "Microscopy and Microanalysis Vol. 7(02): 200–
575   210

577   41. Mitchell, JK. (2005) "Fundamentals of Soil Behavior", 3rd ed. Hoboken, N.J: John
578   Wiley & Sons.

580   42. Newbury, DE., Bright, DS. (1999) "Logarithmic 3-band color encoding: a robust
581   method for display and comparison of compositional maps in electron probe X-ray
582   microanalysis" Microscopy and microanalysis Vol. 5(5): 333–343, doi:
583   10.1017/S1431927699000161

585   43. Oliver, WC., Pharr, GM. (2004) "Measurement of hardness and elastic modulus by
586   instrumented indentation: advances in understanding and refinements to methodology"
587   Journal of Materials Research Vol. 19(1): 3–20, doi: 10.1557/jmr.2004.19.1.3

589   44. Ortega, JA. (2010) "Microporomechanical modeling of shale." PhD dissertation,
590   Massachusetts Institute of Technology, Cambridge.

592   45. Prasad, M., Kopycinska, M., Rabe, U., Arnold, W. (2002) "Measurement of Young's
593   modulus of clay minerals using atomic force acoustic microscopy. " Geophysical
594   Research Letters Vol. 29(8): 13-1–13-4, doi:10.1029/2001GL014054

596   46. Prasad, M., Mukerji, T. (2003) "Analysis of Microstructural Textures And Wave
597   Propagation Characteristics In Shales" SEG Annual Meeting, 26-31 October, Dallas,
598   Texas.

600   47. Prasad, M., Mukerji, T., Reinstaedler, M., Arnold, W. (2009) "Acoustic signatures,
601   impedance microstructure, textural scales, and anisotropy of kerogen-rich shales" SPE
602   Annual Technical Conference and Exhibition, 4-7 October, New Orleans, Louisiana,
603   doi:10.2118/124840-MS

605   48. Randall, NX., Vandamme, M., Ulm, F-J. (2009) "Nanoindentation analysis as a two-
606   dimensional tool for mapping the mechanical properties of complex surfaces" Materials
607   Research Society Vol. 24(3), 679–690, doi: 10.1557/jmr.2009.0149

608   49. Reed, SJB. (2006) "Electron microprobe analysis and scanning electron microscopy
609   in geology" 2nd edn. Cambridge University Press, Cambridge
610

611 50. Tovey, NK., Krinsley, DH. (1991) "Mineralogical mapping of scanning electron
612 micrographs." Sedimentary Geology Vol. 75(1–2): 109–123, doi:10.1016/0037-
613 0738(91)90053-G
614
615 51. Tovey, NK., Krinsley, DH., Dent, DL., Corbett, WM. (1992) "Techniques to
616 quantitatively study the microfabric of soils. " Geoderma Vol. 53(3–4): 217–235,
617 doi:10.1016/0016-7061(92)90056-D
618
619 52. Ulm, F-J., Abousleiman, Y. (2006) "The nanogranular nature of shale. " Acta
620 Geotechnica Vol. 1(2): 77–88, doi: 10.1007/s11440-006-0009-5
621
622 53. Ulm, F-J., Delafargue, A., Constantinides, G. (2005) "Experimental
623 microporomechanics. " In: Dormieux, L., Ulm, F-J. (eds) "Applied micromechanics of
624 porous materials. " Springer, Wien, pp 207–288
625
626 54. Ulm, F-J., Vandamme, M., Bobko, C. P., Ortega, J. A., Tai, K., Ortiz, C. (2007)
627 "Statistical Indentation Techniques for Hydrated Nanocomposites: Concrete, Bone, and
628 Shale. " Journal of American Ceramic Society Vol. 90(9): 2677-2692,
629 doi:10.1111/j.1551-2916.2007.02012.x
630
631 55. Vernik, L., Landis, C. (1996). "Elastic anisotropy of source rocks: Implications for
632 hydrocarbon generation and primary migration" AAPG Bulletin, Vol. 80(4): 531– 544
633
634 56. Vernik, L., and Nur, A. (1992) "Ultrasonic velocity and anisotropy of hydrocar- bon
635 source rocks" Geophysics, Vol. 57: 727–735.
636
637 57. Voltolini, M., Wenk, H-R., Mondol, NH., Bjorlykke, K., Jahren, J. (2009)
638 "Anisotropy of experimentally compressed kaolinite–illite–quartz mixtures." Geophysics
639 Vol. 74(1): D13–D23, doi:10.1190/1.3002557
640
641 58. World Energy Council. (2007) "Survey of energy resources. Technical report. "
642 World Energy Council
643
644 59. Zargari, S., Prasad, M., Mba, K., Mattson, E. (2011) "Organic maturity, hydrous
645 pyrolysis, and elastic property in shales. " Canadian unconventional resources
646 conference, Calgary, November 15–17, SPE 149403, doi: 10.2118/149403-MS
647
648 60. Zhang, G., Wei, Z., Ferrell, RE. (2009) "Elastic modulus and hardness of muscovite
649 and rectorite determined by nanoindentation. " Apllied Clay Sciences Vol. 43(2): 271–
650 281, doi:10.1016/j.clay.2008.08.010
651
652 61. Zhang, G., Wei, Z., Ferrell, RE., Guggenheim, S., Cygan, RT., Luo, J. (2010)
653 "Evaluation of the elasticity normal to the basal plane of non-expandable 2:1
654 phyllosilicate minerals by nanoindentation. " American Mineralogist Vol. 95(5–6): 863–
655 869, doi: 10.2138/am.2010.3398
656

657
658
659
660
661   Figures:

662

663   Figure 1. Multiscale structure-model of organic-rich shale. Level 0 corresponds to the
664   scale of elementary clay particles at nanometer length scales. Level I is a porous
665   clay/kerogen composite at the scale of micrometer (scale of indentation and advanced
666   observational methods such as SEM and EDX), with the porosity representing the
667   mesoporosity. Level II is the scale of porous organic/inorganic hard inclusion composite.

668

669   Figure 2. A typical load versus depth curve obtained by nanoindentation on an organic-
670   rich shale. The indentation hardness, H, and indentation modulus, M, are obtained from
671   the curve.

672

673   Figure 3. Monte Carlo simulation (run on CASINO) displaying electron trajectories in
674   EPMA experiment [13]. The trajectories represented by red color (reaching to 0.5
675   microns of depth) are mostly back-scattered electrons. Trajectories beyond 0.5 are related
676   to low and high energies.

677

678   Figure 4. (a) Clustering analysis of grid indentation data (M,H) only. Phase 1 and 2
679   represent active mechanical phases. (b) Plots showing the mean mechanical properties
680   and volume fractions of each of the identified phases [Haynesville].

681   Figure 5. (a) Chemo-mechanical phase identification from the clustering analysis
682   incorporating both chemical data (Si, Al) and mechanical data (M,H). (b) Plots showing
683   the mean mechanical properties and auto-scaled elemental intensities of the 2 chemical
684   elements (used in clustering) in each of the identified phases [Haynesville]. Phase 1 is
685   identified as a "clay-rich" phase. Similarly, phases 3 and 4 are identified as "calcite-rich"
686   and "quartz-rich" phases, respectively; whereas phase 2 is classified as a mixture phase at
687   the interface between clay-rich and calcite-rich regions.

688   Figure 6. (a) Grid spatial distribution of different material phases detected by clustering
689   analysis of just mechanical data from indentation. White cells represent points with
690   irregular nanoindentation response which are not considered in the analysis. (b) Spatial
691   distribution of different material phases detected by clustering analysis, incorporating
692   both the chemical and mechanical data. [Haynesville].

693   Figure 7. Average volume fraction of clay-rich phase as a function of number of grids.
694   The dashed red line represents the average of all 17 grids.

695   Figure 8. SEM images of Haynesville shale sample at two different magnifications
696   showing the distribution of kerogen in the clay phase.

697   Figure 9. Mean phase properties of clay/kerogen-rich phase: Indentation modulus versus
698   hardness. Haynesville, Marcellus and Fayetteville samples are mature samples, whereas
699   Barnett and Antrim are immature samples. X1 and X3 stand for indentation into the
700   bedding plane and normal-to-bedding plane, respectively.

701   Figure 10. Functional relations between mechanical phase properties (M, H) and (a-b)
702   clay packing density. (c-d) kerogen volume fraction. The kerogen volume fraction η_k was
703   determined from TOC, assuming a constant kerogen density of $\rho_k = 1.2$ g/cc and
704   considering that organic matter is mainly concentrated in the clay phase; whereas the clay
705   packing density was obtained from $\eta_c = 1 - (\eta_k + \phi)$, where ϕ is the porosity. Trend
706   lines are to guide the eyes.

707   Figure 11. Indentation-modulus-to-hardness ratio vs (a) clay packing, and (b) kerogen
708   content.   The kerogen volume fraction η_k was determined from TOC, assuming a
709   constant kerogen density of $\rho_k = 1.2$ g/cc and considering that organic matter is mainly
710   concentrated in the clay phase; whereas the clay packing density was obtained from
711   $\eta_c = 1 - (\eta_k + \phi)$, where ϕ is the porosity. The inlet shows the crossplot of η_k vs. η_c.
712   Trend lines are to guide the eyes. X1 and X3 stand for indentation into the bedding plane
713   and normal-to-bedding plane, respectively.

714
715
716
717
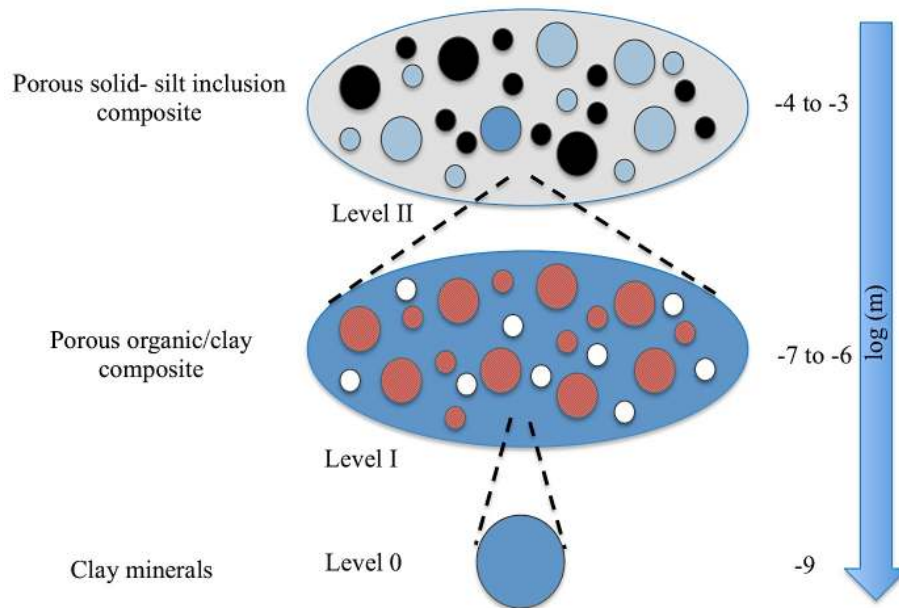
718
719
720 Figure 1. Multiscale structure-model of organic-rich shale. Level 0 corresponds to the scale of elementary clay particles at nanometer
721 length scales. Level I is a porous clay/kerogen composite at the scale of micrometer (scale of indentation and advanced observational
722 methods such as SEM and EDX), with the porosity representing the mesoporosity. Level II is the scale of porous organic/inorganic
723 hard inclusion composite.
724
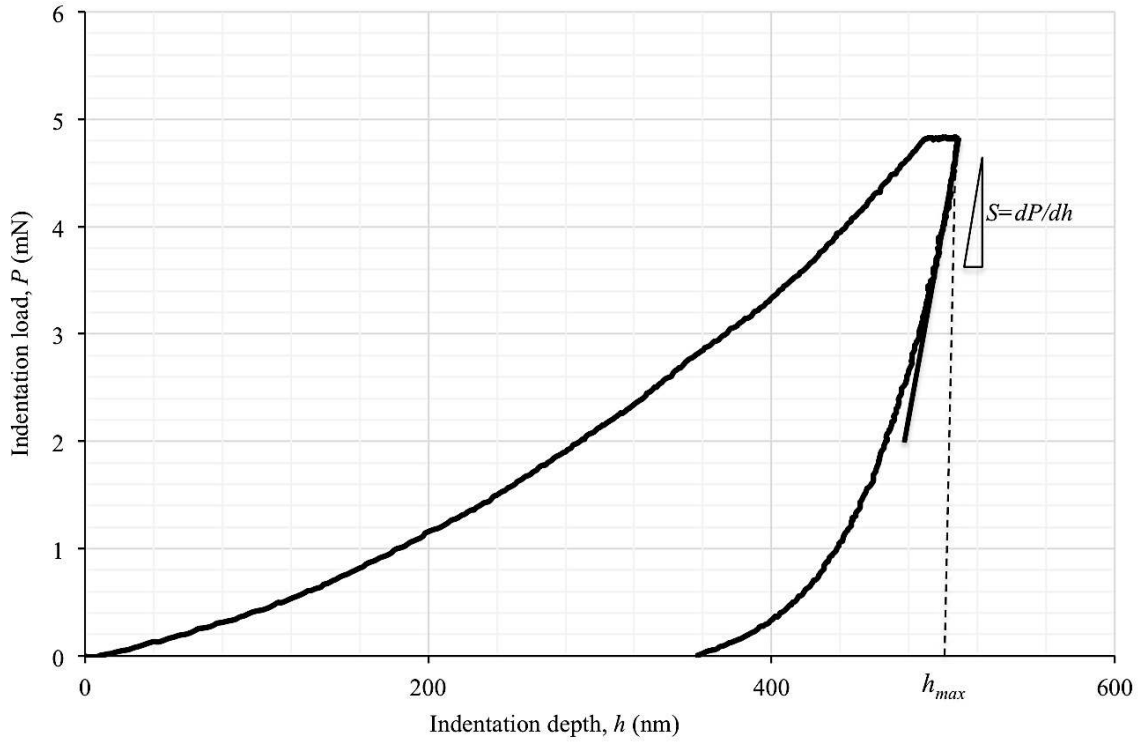
725
726

727
728
729
730

Figure 2. A typical load versus depth curve obtained by nanoindentation on an organic-rich shale. The indentation hardness, H, and indentation modulus, M, are obtained from the curve.

731
732
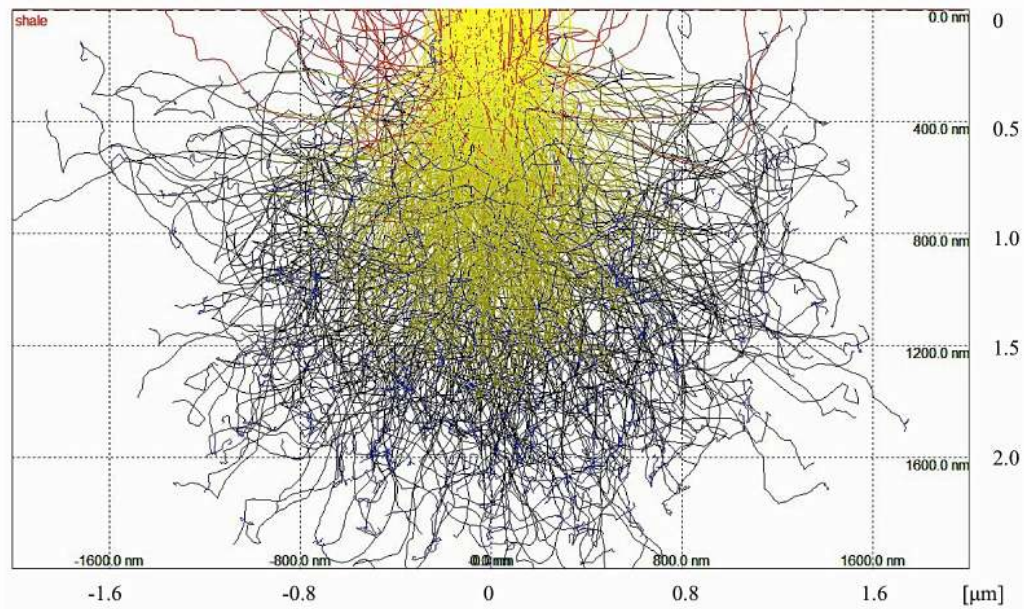
733
734
735
736
737

Figure 3. Monte Carlo simulation (run on CASINO) displaying electron trajectories in EPMA experiment [13]. The trajectories represented by red color (reaching to 0.5 microns of depth) are mostly back-scattered electrons. Trajectories beyond 0.5 are related to low and high energies.
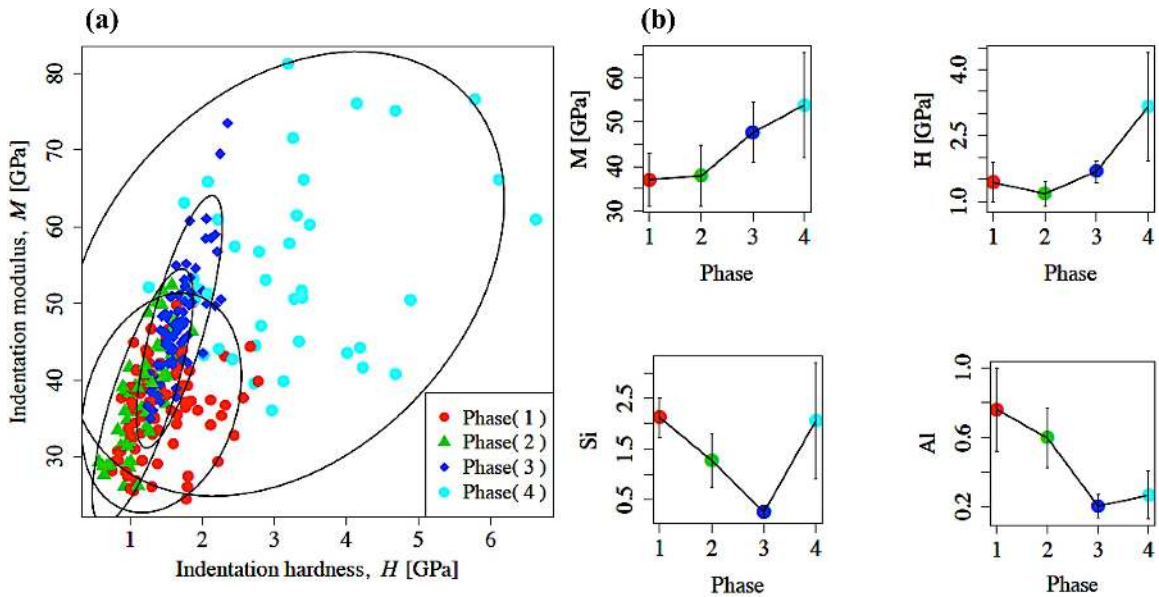
738
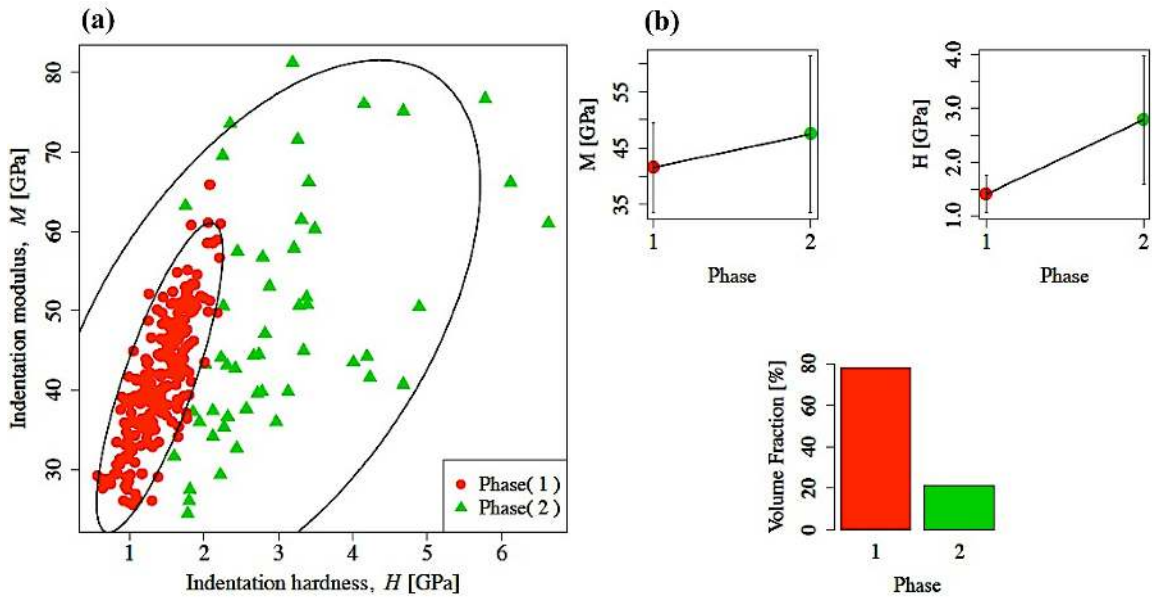
739
740
741 Figure 4. (a) Clustering analysis of grid indentation data (M,H) only. Phase 1 and 2 represent active mechanical phases. (b) Plots
742 showing the mean mechanical properties and volume fractions of each of the identified phases [Haynesville].

743

744
745 Figure 5. (a) Chemo-mechanical phase identification from the clustering analysis incorporating both chemical data (Si, Al) and
746 mechanical data (M,H). (b) Plots showing the mean mechanical properties and auto-scaled elemental intensities of the 2 chemical
747 elements (used in clustering) in each of the identified phases [Haynesville]. Phase 1 is identified as a "clay-rich" phase. Similarly,
748 phases 3 and 4 are identified as "calcite-rich" and "quartz-rich" phases, respectively; whereas phase 2 is classified as a mixture phase
749 at the interface between clay-rich and calcite-rich regions.

750
751
752
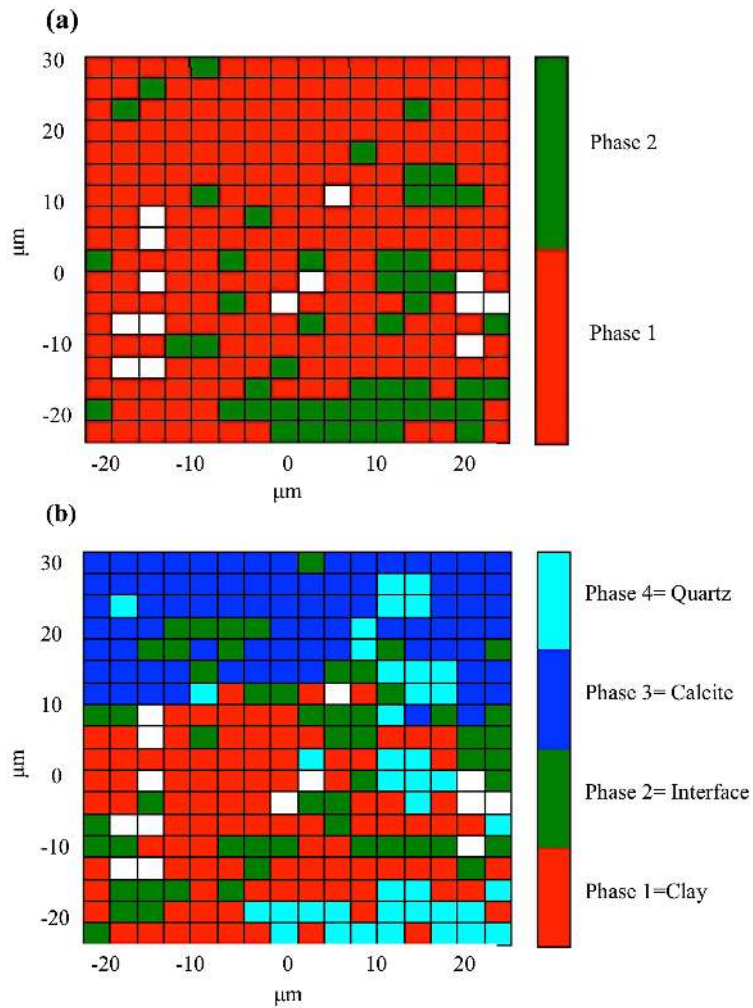
Figure 6. (a) Grid spatial distribution of different material phases detected by clustering analysis of just mechanical data from indentation. White cells represent points with irregular nanoindentation response which are not considered in the analysis. (b) Spatial distribution of different material phases detected by clustering analysis, incorporating both the chemical and mechanical data. [Haynesville].
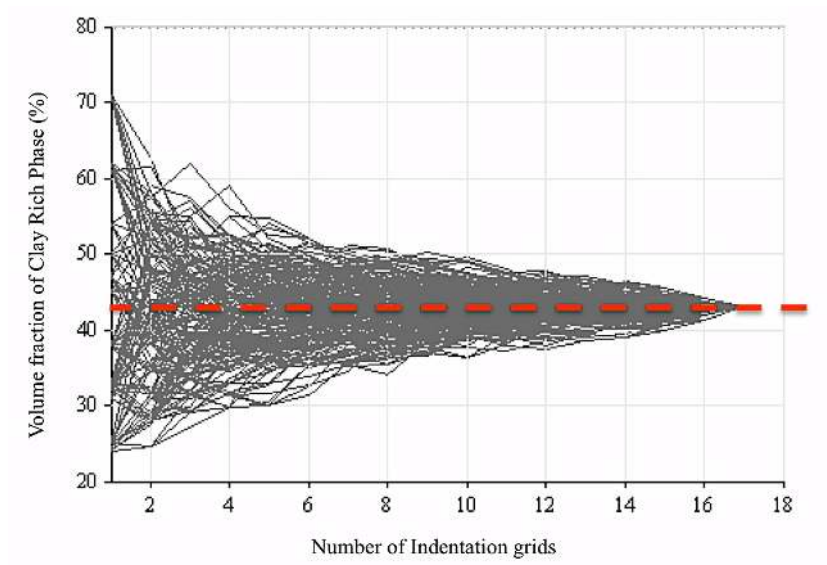
774
775
776 Figure 7. Average volume fraction of clay-rich phase as a function of number of grids. The dashed red line represents the average of
777 all 17 grids.

778
779
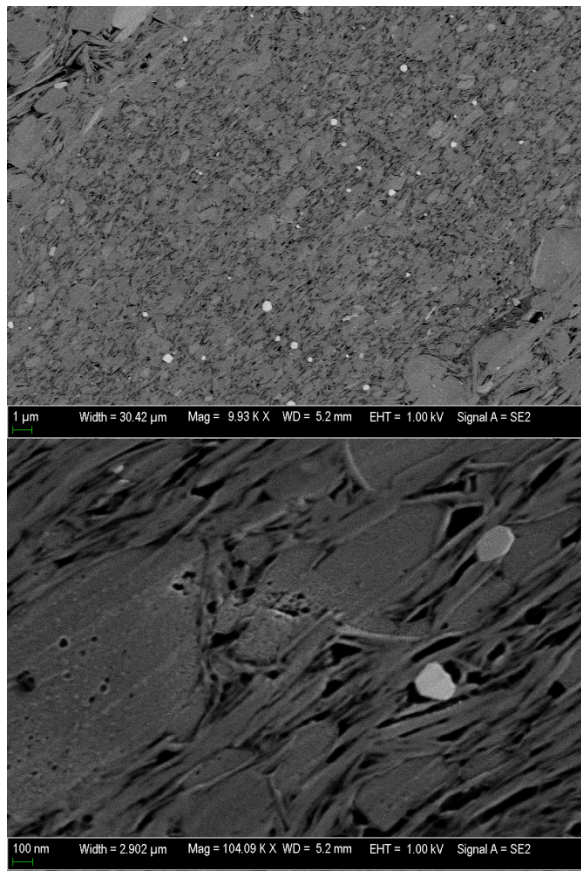
780
781

782
783 Figure 8. SEM images of Haynesville shale sample at two different magnifications showing the distribution of kerogen in the clay
784 phase.
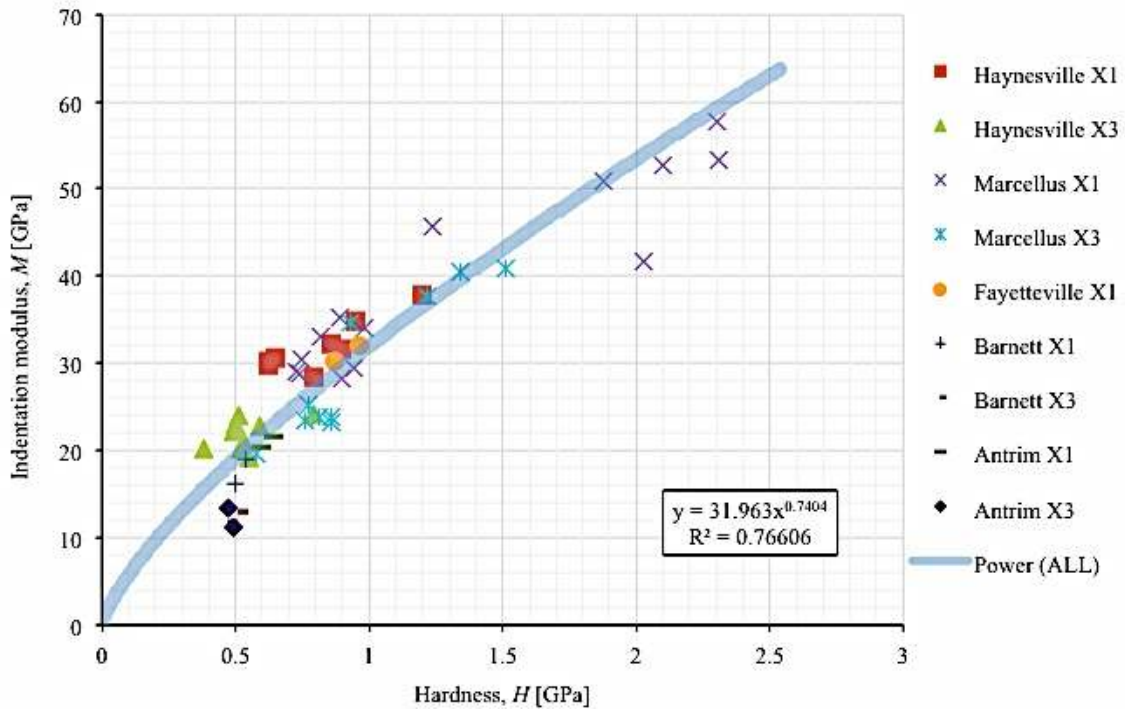
Figure 9. Mean phase properties of clay/kerogen-rich phase: Indentation modulus versus hardness. Haynesville, Marcellus and Fayetteville samples are mature samples, whereas Barnett and Antrim are immature samples. X1 and X3 stand for indentation into the bedding plane and normal-to-bedding plane, respectively.
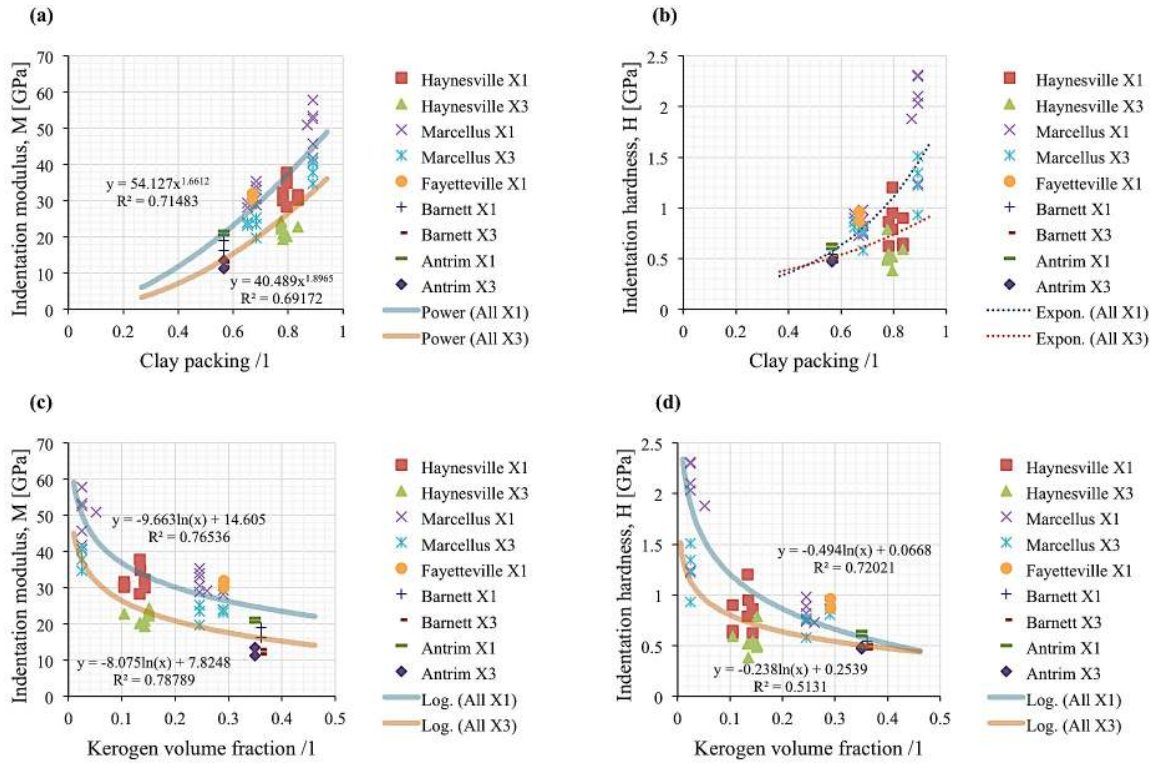
Figure 10. Functional relations between mechanical phase properties (M, H) and (a-b) clay packing density. (c-d) kerogen volume fraction. The kerogen volume fraction η_k was determined from TOC, assuming a constant kerogen density of $\rho_k = 1.2$ g/cc and considering that organic matter is mainly concentrated in the clay phase; whereas the clay packing density was obtained from $\eta_c = 1 - (\eta_k + \phi)$, where ϕ is the porosity. Trend lines are to guide the eyes.
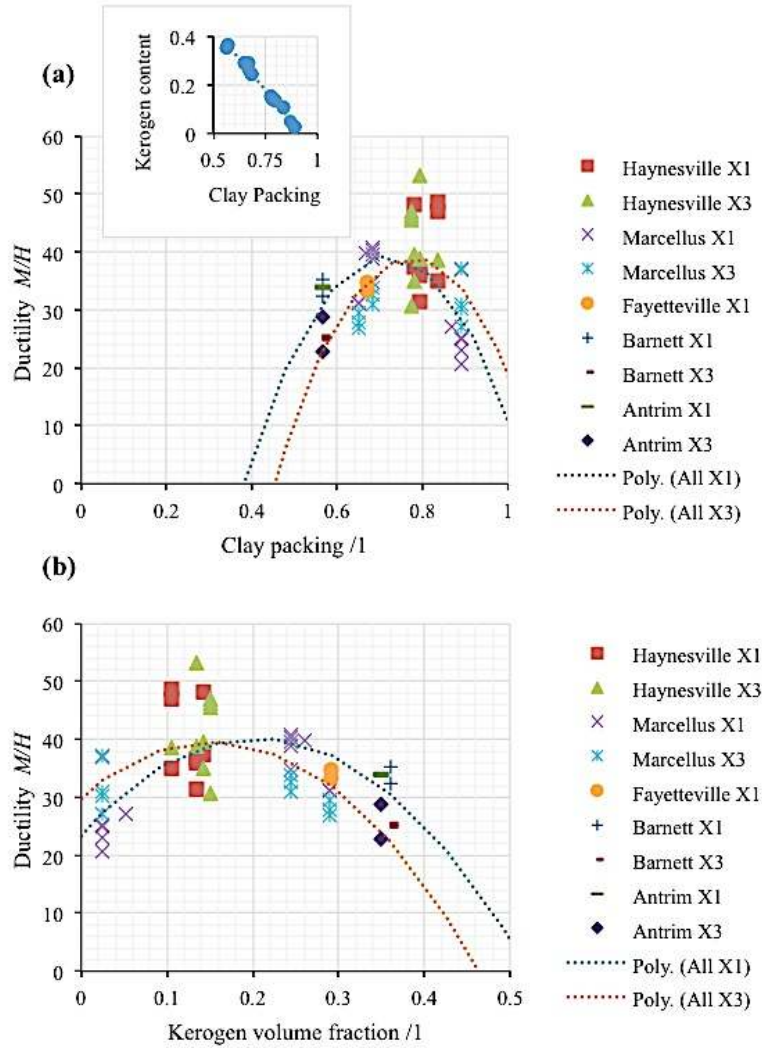
Figure 11. Indentation-modulus-to-hardness ratio vs (a) clay packing, and (b) kerogen content. The kerogen volume fraction η_k was determined from TOC, assuming a constant kerogen density of $\rho_k = 1.2$ g/cc and considering that organic matter is mainly concentrated in the clay phase; whereas the clay packing density was obtained from $\eta_c = 1 - (\eta_k + \phi)$, where ϕ is the porosity. The inlet shows the crossplot of η_k vs. η_c. Trend lines are to guide the eyes. X1 and X3 stand for indentation into the bedding plane and normal-to-bedding plane, respectively.

816   Table 1. Mineralogy, porosity and TOC measurements of the studied samples[a]

817

Sample group	Clay (mass%)	Quartz (mass%)	Carbonates (mass%)	TOC (wt. %)	Porosity (%)
Haynesville	38-45	27-32	9-22	2.6-3.3	6-7.6
Marcellus1	38.9-39.9	18.7-19.7	35.5-37	0.5-1	7.9-8.4
Marcellus2	41.2-48.6	29.4-36.2	4.8-16.1	7.32-8.18	5.9-7.2
Fayetteville	25.1	28.8	31.7	4.9	4
Barnett	41.8	29.7	2.6	12.2	7.3
Antrim	31.41	40.9	4.4	9.6	8.8

818   [a]The mineralogy data were obtained by XRD (courtesy of Shell).

819

820   Table 2. Volume fraction of different material phases present in the studied samples.

821

Sample group	Clay (vol.%)	Quartz (vol.%)	Carbonates (vol.%)	Kerogen (vol.%)
Haynesville	33.1-39.9	23.5-28.1	7.7-18.7	5-6.4
Marcellus1	35.4-36.5	17.3-18.4	32-33.1	1-2.1
Marcellus2	34.1-40.1	24.8-30.4	3.8-13.1	13.6-15.2
Fayetteville	22.7	26.1	27.6	9.85
Barnett	33.4	23.9	2.1	21.4
Antrim	24.5	34.4	3.4	16

822

823

824   Table 3. Volume fraction of kerogen in the clay-rich phase of the studied samples.

825

Sample	Haynesville	Marcellus-1	Marcellus-2	Fayetteville	Barnett	Antrim
η_k	10.5-15	2.5-5.2	24.3-28.8	29.1	34.4	32

826

827

828

829

830

831

832

833

834

835

836

837 Table 4. Summary of the indentation results of clay/kerogen phases in all studied samples[b] μ, σ, and f_c
838 correspond to the mean value, standard deviation, and surface fraction of the clay-rich/kerogen phase.
839

Grid number	Number of indents in the grid	M^μ [GPa]	M^σ [GPa]	H^μ [GPa]	H^σ [GPa]	$f_c(\%)$
Haynesville-X1-1	362	30.58	7.09	0.65	0.20	25
Haynesville-X1-2	409	30.20	5.43	0.62	0.14	38
Haynesville-X1-3	420	31.60	4.51	0.90	0.17	54
Haynesville-X1-4	419	28.36	6.89	0.79	0.33	33
Haynesville-X1-5	280	37.79	5.00	1.20	0.20	24
Haynesville-X1-6	426	34.90	6.14	0.95	0.20	38
Haynesville-X1-7	381	29.94	7.05	0.62	0.25	47
Haynesville-X1-8	416	32.24	6.56	0.86	0.23	38
Haynesville-X3-1	286	22.85	7.75	0.59	0.26	71
Haynesville-X3-2	412	20.20	5.61	0.38	0.15	38
Haynesville-X3-3	435	20.17	5.43	0.52	0.20	45
Haynesville-X3-4	404	20.94	5.92	0.53	0.23	61
Haynesville-X3-5	396	19.28	4.84	0.55	0.24	62
Haynesville-X3-6	167	23.11	6.17	0.50	0.19	45
Haynesville-X3-7	467	22.32	6.42	0.49	0.26	32
Haynesville-X3-8	327	24.33	4.12	0.79	0.18	50
Haynesville-X3-9	346	24.02	6.54	0.51	0.22	31
Marcellus1-X1-1	447	45.74	9.81	1.24	0.51	34
Marcellus1-X1-2	402	41.70	6.32	2.03	0.57	36
Marcellus1-X1-3	363	53.37	7.32	2.31	0.66	32
Marcellus1-X1-4	423	52.61	7.83	2.10	0.78	23
Marcellus1-X1-5	429	57.70	7.12	2.30	0.40	48
Marcellus1-X1-6	435	50.94	9.01	1.88	0.60	36

840 [b]μ, σ, and f_c correspond to the mean value, standard deviation, and surface fraction of the clay-rich/kerogen
841 phase.
842
843

844
845   Table 4 continue. Summary of the indentation results of clay/kerogen phases in all studied samples[b]
846

Grid number	Number of indents in the grid	M^{μ} [GPa]	M^{σ} [GPa]	H^{μ} [GPa]	H^{σ} [GPa]	f_c(%)
Marcellus1-X3-1	402	34.59	8.31	0.93	0.40	30
Marcellus1-X3-2	318	40.95	9.61	1.51	0.63	49
Marcellus1-X3-3	368	37.74	6.41	1.22	0.51	19
Marcellus1-X3-4	369	40.50	8.11	1.34	0.62	24
Marcellus2-X1-1	366	28.81	5.04	0.74	0.18	66
Marcellus2-X1-2	362	35.30	6.39	0.89	0.18	48
Marcellus2-X1-3	360	33.02	5.76	0.82	0.15	49
Marcellus2-X1-4	368	30.52	5.59	0.75	0.16	44
Marcellus2-X1-5	331	34.06	7.23	0.98	0.27	39
Marcellus2-X1-6	363	29.10	5.55	0.73	0.15	37
Marcellus2-X1-7	371	28.17	5.39	0.90	0.21	50
Marcellus2-X1-8	369	29.41	5.50	0.94	0.18	51
Marcellus2-X3-1	383	19.66	3.44	0.58	0.12	34
Marcellus2-X3-2	407	25.17	4.48	0.77	0.19	47
Marcellus2-X3-3	354	23.51	4.24	0.76	0.16	51
Marcellus2-X3-4	371	23.85	6.22	0.81	0.29	57
Marcellus2-X3-5	390	23.92	5.28	0.86	0.23	53
Marcellus2-X3-6	381	23.19	5.51	0.86	0.29	36
Fayetteville-X1-1	383	31.99	5.91	0.96	0.21	56
Fayetteville-X1-2	389	30.27	6.05	0.87	0.18	30

847   [b]μ, σ, and f_c correspond to the mean value, standard deviation, and surface fraction of the clay-rich/kerogen
848   phase.
849
850
851
852
853
854
855

Table 4 continue. Summary of the indentation results of clay/kerogen phases in all studied samples[b]

Grid number	Number of indents in the grid	M^μ [GPa]	M^σ [GPa]	H^μ [GPa]	H^σ [GPa]	$f_c(\%)$
Barnett-X1-1	471	18.99	4.56	0.54	0.09	31
Barnett-X1-2	475	16.19	3.07	0.50	0.08	41
Barnett-X3-1	466	11.78	2.45	0.47	0.08	47
Barnett-X3-2	461	12.97	1.87	0.51	0.08	31
Antrim-X1-1	479	21.60	5.33	0.64	0.13	41
Antrim-X1-2	475	20.49	3.58	0.60	0.10	33
Antrim-X3-1	402	13.49	3.06	0.47	0.11	43
Antrim-X3-2	354	11.16	2.40	0.49	0.12	36

858   [b]μ, σ, and f_c correspond to the mean value, standard deviation, and surface fraction of the clay-rich/kerogen
859   phase.
860

accounts for inorganic elements. That is, the phases thus identified will certainly include the organic phases as well."

REVIEW: What are the clay mineral types in the different samples?

- AUTHORS' REPLY: Clay minerals in these samples were mostly either illite or mixed illite-smectite, with relatively smaller amounts of kaolinite and chlorite.
- ACTION TAKEN: We have added the above sentence to the revised version of the manuscript for clarification.

REVIEW:
- How did the authors determine dry bulk density?
- drying oil window samples will drive out S1 hydrocarbons
- Is dry density with or without clay-bound waters? Haynesville rocks have considerable amounts of swelling clays: heating temperature will play a big role.

- AUTHORS' REPLY: The temperature that was used for drying the samples was 60° C which is much lower that the temperature that causes the evaporation of clay-bound water and also extraction of S1 hydrocarbons. The above claim is supported by the following references:
- Killops, S., Killops, V. (2005) "Introduction to organic geochemistry" Blackwell Publishing, Malden, MA.
- Saeedi, A. (2012) "Experimental Study of Multiphase Flow in Porous Media during CO2 Geo-Sequestration Processes" Springer Thesis Series, Heidelberg, Germany, Springer Publishing.

REVIEW: Need Rock-eval data or another measure of the produced and trapped hydrocarbons.

- AUTHORS' REPLY: Our Rock-eval data does not provide the amount of produces and hydrated hydrocarbons. However, since the focus of the paper is nanomechanics of porous clay/kerogen phases, the role of produced and trapped hydrocarbons is considered minor compared to TOC, porosity, volume fraction of clay, and state of maturity.

REVIEW: The assumption of kerogen only being associated with clay minerals is not justified.

- AUTHORS' REPLY: This assumption is supported by several papers such as Vernik and Nur, 1992; Kuila et al., 2014, and Fitzgerald et al., 1989.
- ACTION TAKEN: We have added these citations to the revised version of the manuscript. Moreover, Figure 8 in the revised version of the manuscript